


Dynamics and energetics underlying mixing efficiency in homogeneous stably stratified turbulence

Young R. Yi * and Jeffrey R. Koseff

*Bob and Norma Street Environmental Fluid Mechanics Laboratory,
Department of Civil and Environmental Engineering, Stanford University, Stanford, California 94305, USA*



(Received 24 January 2022; accepted 21 July 2022; published 12 August 2022)

We studied homogeneous stably stratified turbulence in a triply periodic domain over a wide range of stratification strengths. We evaluated the statistically stationary, volume-averaged budgets of Reynolds stresses, turbulent potential energy, and turbulent vertical density flux. By separately studying the three components of the turbulent kinetic energy (TKE), we examined the role of pressure-strain correlations and observed connections between changes in the energetics to regime shifts of the mixing coefficient (Γ) as a function of the turbulent Froude number (Fr_t). As we increase stratification, we find that pressure-strain correlations become more important in producing the vertical component of TKE (k_w). At the stratification strength where direct production and pressure-strain correlations equally generate k_w , we observe the maximum value of Γ , and it remains constant as stratification is increased further. However, when we greatly increase stratification from this point, the pressure-strain correlations become the dominant source of k_w with direct production becoming negligible, and this change is accompanied by the mixing coefficient decreasing from its maximum value. Finally, we find that this final transition for the mixing coefficient coincides with a sign change of the pressure scrambling term in the vertical density flux budget.

DOI: [10.1103/PhysRevFluids.7.084801](https://doi.org/10.1103/PhysRevFluids.7.084801)

I. INTRODUCTION

The fluid motions of oceanic flows involve a wide range of scales with the winds and tides driving large-scale motions of $O(10^5-10^7\text{ m})$ [1] that eventually get dissipated at viscous scales of $O(1\text{ mm})$ (estimated based on surface ocean measurements from Ref. [2]). Current global climate simulations typically have horizontal and vertical grid scales of $O(10\text{ km})$ and $O(10\text{ m})$, respectively [3], and therefore these simulations rely on subgrid-scale models to represent the effects of unresolved scales that lie between the dissipative (physical) and grid (numerical) scales. For example, down-gradient models are commonly used in global climate simulations to estimate the eddy viscosity of momentum and eddy diffusivity of scalars (see Sec. 2 of Ref. [3]).

Regarding the modeled quantities, significant effort has been expended to accurately represent the subgrid-scale vertical buoyancy flux since it strongly modifies the background density field, therefore affecting the global overturning circulation [4–6]. In particular, ocean models have often used the down-gradient vertical buoyancy flux model by Ref. [7]. Here we provide the nondimensional form of this model from Ref. [8]:

$$\frac{D_T}{D} = \left(\frac{\text{Ri}_f}{1 - \text{Ri}_f} \right) \frac{\epsilon_k}{DN^2} = \Gamma \left(\frac{\epsilon_k}{\nu N^2} \right) \left(\frac{\nu}{D} \right) = \Gamma \text{Re}_b \text{Pr}, \quad (1)$$

*yryi@stanford.edu

where D_T and D are the eddy and molecular diffusivities of the stratifying scalar field; Ri_f is the mixing efficiency or flux Richardson number, broadly representing the fraction of the energy input that is used to irreversibly mix the stratifying scalar field; $\Gamma = Ri_f/(1 - Ri_f)$ is the mixing coefficient; ϵ_k is the dissipation rate of turbulent kinetic energy; ν is the kinematic viscosity of the fluid; $N^2 = -(g/\rho_0)d_z\bar{\rho}$ is the vertical background stratification; $Re_b = \epsilon_k/(\nu N^2)$ is the buoyancy Reynolds number, often interpreted as a measure of the intensity of a stratified turbulent flow; and $Pr = \nu/D$ is the molecular Prandtl number. Reference [9] provides further discussion and quantitative comparisons of various definitions of the flux Richardson number, and Ref. [10] presents necessary modifications for defining a mixing efficiency for unsteady, inhomogeneous stably stratified flows.

A major strength of Eq. (1) is its ease of application. The molecular Prandtl number is well known, and ϵ_k and N^2 can be measured in the field using microstructure and CTD (e.g., Ref. [11]), giving an estimate of the buoyancy Reynolds number. The final piece, then, involves estimating either the flux Richardson number or the mixing coefficient in terms of known or easily measurable quantities. This issue is well summarized by Refs. [12–15]. In this vein, [16] studied the relationship between Ri_f and Re_b using a synthesis of laboratory experiments, field measurements, and numerical simulations of different types of stably stratified turbulent flows. Most datasets exhibited a constant value of Ri_f for $Re_b < 100$ and $Ri_f \sim Re_b^{-1/2}$ for $Re_b > 100$, but there were some datasets that exhibited this transition at much larger values of Re_b than 100. Reference [17] theoretically formulated and tested a different parametrization of the mixing coefficient in terms of the turbulent Froude number $Fr_k = \epsilon_k/(Nk)$, where k is the turbulent kinetic energy. While obtaining field estimates of Fr_k is more challenging than measuring Re_b due to the need to measure k , the Garanaik and Venayagamoorthy (GV) formulation ostensibly collapsed data from decaying and forced, stably stratified, homogeneous turbulence as well as from sheared, stably stratified, homogeneous turbulence. In a related study, using a set of forced stably stratified homogeneous turbulence simulations at a fixed value of Re_b , [18] showed that Γ depends primarily on Fr_k and hypothesized that revisiting existing datasets of Γ and plotting them in terms of Fr_k rather than Re_b would result in better collapse. We suspect that their hypothesis is helpful in explaining the nonunique relationships between Ri_f and Re_b reported by Ref. [16], and is also most helpful in explaining the apparent disagreement between the findings of Refs. [19,20] on how Γ is related to Re_b for sheared, stably stratified, homogeneous turbulence.

As a result of these recent studies, the expected shapes of Ri_f or Γ as a function of Fr_k appear to be well established, although what happens exactly as $Fr_k \rightarrow 0$ is still disputed [14]. Missing in all of this, however, is a clear physical understanding of what quantifiable differences exist among stably stratified turbulent flows occupying the different Fr_k -scaling regimes identified by Refs. [17,18]. To address this need, we conducted a set of direct numerical simulations (DNS) of linearly forced, stably stratified, homogeneous turbulence with the goal of clearly connecting the relationship of Γ and Fr_k to the extant physics of this flow. Specifically, we seek to identify links between Γ and notable changes in the vertical Reynolds stress and density flux budgets in terms of Fr_k .

Our paper is organized as follows: governing equations, related second-moment equations, and solution methodology are discussed in Sec. II; simulation results as a function of Fr_k and an alternative formulation of Ri_f with some remarks on Reynolds number effects are presented in Sec. III; and concluding remarks are provided in Sec. IV.

II. PROBLEM SETUP AND METHODOLOGY

A. Equations of motion and second-moment budgets

In this study, we use the incompressible, Navier-Stokes equations under the Boussinesq approximation with linear velocity forcing [21,22]:

$$\frac{\partial u_j}{\partial x_j} = 0, \quad (2)$$

$$\frac{\partial u_j}{\partial t} + u_m \frac{\partial u_j}{\partial x_m} = -\frac{1}{\rho_0} \frac{\partial p}{\partial x_j} - \frac{g}{\rho_0} \rho \delta_{j3} + \nu \frac{\partial^2 u_j}{\partial x_m \partial x_m} + Au_j, \quad (3)$$

$$\frac{\partial \rho}{\partial t} + u_m \frac{\partial \rho}{\partial x_m} = -w \frac{d\bar{\rho}}{dz} + D \frac{\partial^2 \rho}{\partial x_m \partial x_m}, \quad (4)$$

where u_j , p , and ρ represent velocity, pressure, and density fluctuations, respectively, $\bar{\rho}(z)$ is the stable, linearly varying, background density field ($d_z \bar{\rho} < 0$), g is the gravitational acceleration, ρ_0 is the reference density, ν is the kinematic viscosity of the fluid, D is the molecular diffusivity of density, and A is the momentum forcing rate. Tensor indices (1, 2, 3) correspond to spatial directions (x, y, z) and velocity fields (u, v, w) with gravity acting along the z -axis. Repeated indices imply summation.

The turbulent kinetic energy (TKE, $k = \frac{1}{2} \overline{u_j u_j}$), turbulent potential energy (TPE, $k_p = \frac{1}{2} \alpha^2 \overline{\rho \rho}$), Reynolds stress ($\overline{u_i u_j}$), and density flux ($\overline{u_j \rho}$) equations associated with Eqs. (2)–(4) are

$$\frac{dk}{dt} = 2Ak - \frac{g}{\rho_0} \overline{w \rho} - \nu \frac{\overline{\partial u_j}}{\partial x_m} \frac{\overline{\partial u_j}}{\partial x_m} = P_k - B - \epsilon_k, \quad (5)$$

$$\frac{dk_p}{dt} = \frac{g}{\rho_0} \overline{w \rho} - D \alpha^2 \frac{\overline{\partial \rho}}{\partial x_m} \frac{\overline{\partial \rho}}{\partial x_m} = B - \epsilon_p, \quad (6)$$

$$\frac{d\overline{u_i u_j}}{dt} = 2A\overline{u_i u_j} + \frac{2}{\rho_0} \overline{p s_{ij}} - \frac{g}{\rho_0} (\overline{u_i \rho} \delta_{j3} + \overline{u_j \rho} \delta_{i3}) - 2\nu \frac{\overline{\partial u_i}}{\partial x_m} \frac{\overline{\partial u_j}}{\partial x_m} = P_{ij} + R_{ij} - B_{ij} - \epsilon_{ij}, \quad (7)$$

$$\frac{d\overline{u_j \rho}}{dt} = A\overline{u_j \rho} + \frac{1}{\rho_0} \overline{p \frac{\partial \rho}{\partial x_j}} - \overline{u_j w} \frac{d\bar{\rho}}{dz} - \frac{g}{\rho_0} \overline{\rho \rho} \delta_{j3} - (\nu + D) \frac{\overline{\partial u_j}}{\partial x_m} \frac{\overline{\partial \rho}}{\partial x_m}, \quad (8)$$

where $s_{ij} = \frac{1}{2}(\partial_j u_i + \partial_i u_j)$ is the rate-of-strain tensor associated with the velocity fluctuations, and $\alpha = g/(\rho_0 N)$ is a constant and uniform dimensional factor needed to convert the dimensions of density to those of velocity. In Eqs. (5) and (6), P_k is the rate of production of TKE from linear forcing, B is the buoyancy flux, and ϵ_k and ϵ_p are the dissipation rates of TKE and TPE, respectively. We note that the subscripts k and p indicate quantities associated with TKE and TPE, respectively, and do not indicate tensor indices. In Eq. (7), P_{ij} is the rate of production of the Reynolds stresses from linear forcing, R_{ij} represents the pressure-strain correlations, B_{ij} is a term associated with the buoyancy flux, and ϵ_{ij} represents the dissipation rates of the Reynolds stresses. We use overbars to denote volume averaging, and because our flow is statistically homogeneous in all three spatial directions, the transport terms are exactly zero, leaving only the volume-averaged source and sink terms in Eqs. (5)–(8).

We can further simplify Eqs. (7) and (8) because of the following considerations. First, the linear forcing term in Eq. (3) does not couple the velocity components in different directions (i.e., it does not generate off-diagonal/shear Reynolds stresses). This allows us to only consider the diagonal components of Eq. (7). Second, due to the statistical axisymmetry of our flow about the vertical axis, we further average the two horizontal Reynolds stresses (\overline{uu} , \overline{vv}) together to consider just one budget for the horizontal Reynolds stresses. Finally, because only a mean vertical density gradient is imposed, we only need to consider the $j = 3$ component of Eq. (8). With these simplifications, we rewrite Eqs. (7) and (8) as follows with the TKE (5) and TPE (6) equations repeated for convenience:

$$\frac{dk}{dt} = 2Ak - \frac{g}{\rho_0} \overline{w \rho} - \nu \frac{\overline{\partial u_j}}{\partial x_m} \frac{\overline{\partial u_j}}{\partial x_m} = P_k - B - \epsilon_k, \quad (5)$$

$$\frac{dk_p}{dt} = \frac{g}{\rho_0} \overline{w \rho} - D \alpha^2 \frac{\overline{\partial \rho}}{\partial x_m} \frac{\overline{\partial \rho}}{\partial x_m} = B - \epsilon_p, \quad (6)$$

$$\frac{d\frac{1}{2}\overline{u_H u_H}}{dt} = A\overline{u_H u_H} + \frac{1}{\rho_0} \overline{p s_{HH}} - \nu \frac{\overline{\partial u_H}}{\partial x_m} \frac{\overline{\partial u_H}}{\partial x_m} = P_H + R_H - \epsilon_H, \quad (9)$$

TABLE I. Global input parameters for the numerical simulations.

L_x, L_y, L_z (m)	N_x, N_y, N_z	Δt (s) ^a	ν (m ² /s)	κ (m ² /s)	g (m/s ²)	ρ_0 (kg/m ³)
2π	64	2.5×10^{-3}	5×10^{-2}	5×10^{-2}	9.8	1

^aSimulation V1 used $\Delta t = 1.25 \times 10^{-3}$ s for numerical stability.

$$\frac{d\frac{1}{2}\overline{w\overline{w}}}{dt} = A\overline{w\overline{w}} + \frac{1}{\rho_0}\overline{ps_{33}} - \frac{g}{\rho_0}\overline{w\overline{\rho}} - \nu\overline{\frac{\partial w}{\partial x_m}\frac{\partial w}{\partial x_m}} = P_w + R_w - B - \epsilon_w, \quad (10)$$

$$\frac{d\overline{w\overline{\rho}}}{dt} = A\overline{w\overline{\rho}} + \frac{1}{\rho_0}\overline{p\frac{\partial \rho}{\partial z}} - \overline{w\overline{w}}\frac{d\overline{\rho}}{dz} - \frac{g}{\rho_0}\overline{\rho\overline{\rho}} - (\nu + D)\overline{\frac{\partial w}{\partial x_m}\frac{\partial \rho}{\partial x_m}}. \quad (11)$$

Equations (9) and (10) are the budgets of the horizontal and vertical components of TKE ($k_H = \frac{1}{2}\overline{u_H u_H} = \frac{1}{4}(\overline{uu} + \overline{vv})$, $k_w = \frac{1}{2}\overline{w\overline{w}}$), respectively, where the sum of two times Eqs. (9) and (10) is equivalent to Eq. (5) (i.e., $k = 2k_H + k_w$). Moreover, due to the incompressibility condition (2), the diagonal components of the pressure-strain correlations sum to zero (i.e., $2R_H = -R_w$). Therefore, the pressure-strain correlations do not add or remove TKE but exchange it among its three components in an attempt to bring the normal Reynolds stresses closer in magnitude [23]. For axisymmetric, stably stratified turbulence, we expect the root-mean-square horizontal velocity fluctuations to be larger than their vertical counterpart because the buoyancy flux directly couples only k_w and k_p . Therefore, we expect $R_H < 0$ and $R_w > 0$, indicating a transformation of k_H into k_w . In Sec. III, we evaluate the right-hand side (RHS) terms of Eqs. (5), (6), (9)–(11) as a function of the turbulent Froude number and establish connections to how the mixing coefficient varies with the turbulent Froude number.

B. Numerical solution procedure and nondimensional parameters

We solved Eqs. (2)–(4) for a triply periodic, cubic domain of length $L = 2\pi$ using our own Fourier pseudospectral solver with an RK4 time-stepping scheme. We verified the fourth-order temporal accuracy and nonlinear advection terms by comparing our numerical solutions to the analytical solutions of a decaying Taylor-Green vortex in two dimensions [24]. The density coupling was implicitly verified by observing the correct behavior of the time-varying forcing strategies (further discussed in Sec. III A and Appendix B), which required accurate solutions of Eqs. (2)–(4). Nonlinear terms were dealiased exactly by zero-padding [25]. Additional information about the simulations are provided in Tables I and II.

The nondimensional input parameters of our system are A/N , $\text{Re}_A = AL^2/\nu$, and $\text{Pr} = \nu/D$, where N is the buoyancy frequency. For our simulations, we prescribed a molecular Prandtl number of unity, and we varied A/N to study the effects of increasing stable stratification relative to momentum forcing. Because the value of A varied across our simulations, our input Reynolds number Re_A also varied. Additionally, for the simulations with time-varying A , we note that A/N was not prescribed but was an output parameter. This is because for simulations with a time-varying controller, the user does not specify A , but it is rather an outcome of the simulations.

The nondimensional output parameters of interest of our system are $\text{Re}_b = \epsilon_k/(\nu N^2) = (l_O/\eta_k)^{4/3}$, $\text{Re}_L = k^2/(\nu \epsilon_k) = (l_L/\eta_k)^{4/3}$, $\text{Fr}_k = \epsilon_k/(Nk) = (l_L/l_O)^{-2/3}$, and $\Gamma = \epsilon_p/\epsilon_k$, where $l_L = k^{3/2}/\epsilon_k$, $l_O = (\epsilon_k/N^3)^{1/2}$, and $\eta_k = (\nu^3/\epsilon_k)^{1/4}$ are the large-eddy, Ozmidov, and Kolmogorov scales, respectively. The first three nondimensional parameters are the buoyancy Reynolds number, the large-eddy Reynolds number, and the turbulent Froude number, and they can be interpreted as ratios of turbulence length scales. For $A/N > 1$, Re_L broadly represents the range of isotropic scales (η_k to l_L) given that the Ozmidov length scale is larger than the large-eddy length scale. Therefore, there is a range of scales between l_L and l_O (estimated by Fr_k) that is inactive/physically irrelevant [18], and Re_b overestimates the range of active turbulent length scales. For $A/N < 1$, however,

TABLE II. Nondimensional and control parameters for the set of DNS.

Sim. ^a	A/N^b	Fr_k^b	Re_L^b	Re_b^b	l_O / L^b	$\kappa_{\max} \eta^b$	$k_{\infty}^{b,c}$	$\epsilon_{k,\infty}^{b,c}$	$k_{w,\infty}^{b,c}$	t_s/t_B^d	t_f/t_B^d	u_j^e	ρ^e
C1	0.38	0.66	181.91	75.81	0.27	2.03	7.61	6.74	1.37	3.58	9.95	S	0.1
C2	0.50	0.86	97.09	71.32	0.30	2.39	4.13	3.57	0.93	2.52	9.95	S	0.1
C3	0.93	1.72	103.36	302.71	0.76	2.04	5.85	6.73	1.66	1.35	9.95	S	0.1
C4	1.36	2.59	100.96	669.90	1.33	1.97	6.20	7.68	1.88	0.75	5.00	C8	C8
C5	1.49	2.89	107.47	887.94	1.61	1.92	6.71	8.45	1.99	0.38	4.99	C8	C8
C6	1.95	3.82	106.57	1544.02	2.42	1.92	6.73	8.58	2.12	0.59	4.97	S	0.1
C7	2.28	4.48	109.85	2181.21	3.11	1.90	6.95	8.89	2.22	0.26	5.00	C8	C8
C8	2.60	5.13	106.55	2775.85	3.75	1.91	6.77	8.67	2.25	0.45	4.97	S	0.1
K1	0.42	0.70	135.63	63.28	0.25	2.13	6.00	5.63	1.17	0.52	9.95	S	0.1
K2	0.52	0.90	116.79	91.90	0.31	2.06	6.00	6.36	1.32	0.42	9.95	S	0.1
K3	0.64	1.13	82.21	101.40	0.44	2.68	3.00	2.25	0.71	0.42	9.95	S	0.1
K4	0.67	1.19	102.50	143.23	0.43	2.00	6.00	7.16	1.48	0.36	9.95	S	0.1
K5	0.82	1.48	103.29	222.36	0.59	2.01	6.00	7.12	1.59	0.35	9.95	S	0.1
K6	1.25	2.35	77.17	423.73	1.27	2.65	3.00	2.35	0.87	0.34	4.97	S	0.2
K7	1.28	2.44	99.75	585.89	1.22	1.99	6.00	7.32	1.81	0.28	4.97	S	0.1
K8	1.66	3.22	75.43	772.73	1.98	2.63	3.00	2.41	0.91	0.19	4.97	S	0.1
D1	0.15	0.24	463.70	22.50	0.15	2.76	6.61	2.00	0.57	1.26	35.15	S	0.1
D2	0.25	0.41	234.90	33.75	0.18	2.49	5.80	3.00	0.78	1.13	19.89	S	0.1
D3	0.31	0.51	190.88	45.00	0.21	2.32	6.10	4.00	0.93	0.78	15.25	S	0.1
D4	0.30	0.51	245.21	60.00	0.22	1.98	9.50	7.50	1.46	1.26	15.10	D8	D8
D5	0.39	0.65	131.32	50.63	0.22	2.25	5.36	4.50	1.07	0.68	15.25	S	0.1
D6	0.43	0.73	122.34	60.00	0.25	2.25	5.17	4.50	1.04	0.10	9.99	D8	D8
D7	0.45	0.75	126.11	67.50	0.25	2.09	6.11	6.00	1.30	0.68	20.03	S	0.1
D8	0.47	0.81	135.69	84.38	0.28	1.98	7.08	7.50	1.48	0.74	9.95	S	0.1
D9	0.52	0.89	129.84	100.00	0.32	1.98	6.94	7.50	1.53	0.22	9.99	C8	C8
D10	0.53	0.92	74.90	60.00	0.33	2.96	2.35	1.50	0.52	0.34	9.99	D8	D8
D11	0.57	0.99	104.78	100.00	0.37	2.25	4.84	4.50	1.12	0.22	10.00	C8	C8
D12	0.68	1.20	66.32	91.88	0.45	2.96	2.22	1.50	0.56	0.43	9.95	S	0.1
D13	0.68	1.21	69.93	100.00	0.48	2.96	2.28	1.50	0.54	0.19	10.02	C8	C8
D14	0.84	1.52	81.29	183.75	0.64	2.49	3.48	3.00	0.96	0.43	9.95	S	0.1
D15	0.96	1.78	88.65	275.63	0.78	2.25	4.45	4.50	1.24	0.38	9.95	S	0.1
D16	1.07	2.00	94.36	367.50	0.90	2.09	5.30	6.00	1.53	0.28	9.95	S	0.1
D17	1.12	2.12	104.64	459.38	1.01	1.98	6.24	7.50	1.77	0.28	9.95	S	0.1
D18	1.59	3.09	107.12	1000.02	1.81	1.98	6.31	7.50	1.93	0.027	5.01	C8	C8
D19	1.75	3.42	87.71	1000.00	2.05	2.25	4.42	4.50	1.36	0.045	5.07	C8	C8
D20	1.81	3.53	81.79	1000.00	2.27	2.49	3.49	3.00	1.08	0.078	4.99	C8	C8
V1	0.010	0.016	34673.91	9.34	0.034	1.25	283.52	46.69	1.30	17.51	60.68	S	0.1
V2	0.019	0.032	11771.82	12.13	0.048	1.44	124.81	26.95	1.30	8.75	50.40	S	0.1
V3	0.031	0.051	5620.83	14.07	0.060	1.60	69.37	17.58	1.30	8.75	40.29	S	0.1
V4	0.060	0.10	2044.58	18.65	0.084	1.83	31.75	10.36	1.30	5.01	30.17	S	0.1
V5	0.10	0.17	989.35	25.60	0.11	1.95	19.53	8.00	1.30	5.02	25.12	S	0.1
V6	0.15	0.25	609.54	36.11	0.15	2.00	14.65	7.22	1.30	2.51	15.12	S	0.1

^aconstant A (C series), constant k (K series), constant ϵ_k (D series), constant k_w (V series).

^bBolded quantities are prescribed. Otherwise, values are volume and time averaged.

^cTargets for time-varying forcing strategies. See Sec. III A and Appendix B for more information.

^dNormalized start and end times of temporal averaging windows with $t_B = 2\pi/N$.

^eChoice of velocity and density initial conditions. More information is provided in Appendix A.

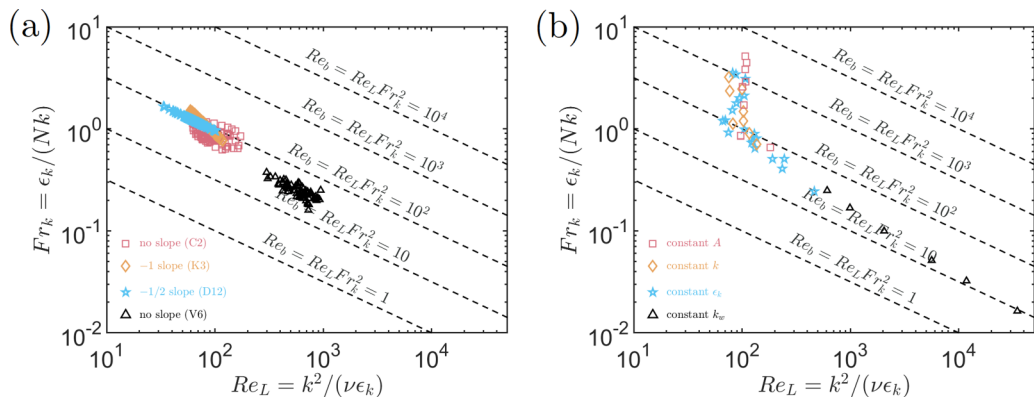


FIG. 1. (a) Temporal trajectories of volume-averaged values of Re_L and Fr_k for four simulations with different temporal forcing strategies: constant A (red squares), constant k (orange diamonds), constant ϵ_k (blue stars), constant k_w (black triangles). The four simulations only correspond to the C2, K3, D12, and V6 simulations in Table II. (b) Volume- and time-averaged values of Re_L and Fr_k for all simulations in Table II.

Re_b now represents the range of isotropic scales (η_k to l_O) because the Ozmidov length scale is smaller than the large-eddy length scale, and Fr_k represents the range of anisotropic scales (l_O to l_L). For this regime, Re_L now represents information about both the isotropic and anisotropic range of scales. Therefore, one needs to carefully interpret the physical significance of Re_b and Re_L depending on whether $A/N < 1$ or $A/N > 1$. For simulations with time-varying A with $\epsilon_k = \epsilon_{k,\infty}$, which represents some desired/target constant value of the TKE dissipation rate, we note that $Re_b = Re_{b,\infty} = \epsilon_{k,\infty} / (\nu N^2)$ becomes an input parameter. The final nondimensional parameter is the mixing coefficient $\Gamma = \epsilon_p / \epsilon_k$, which is the ratio of the dissipation rates of TPE and TKE, and notably, it appears as an unknown in the Osborn eddy diffusivity model in Eq. (1). In the following section, we study how Γ varies with Fr_k and connect its different Fr_k scalings to notable shifts in the budgets described by Eqs. (9)–(11).

III. RESULTS

A. Different temporal forcing strategies

We choose the momentum forcing coefficient, A , to either be constant or vary in time. For the constant forcing simulations, all turbulence statistics vary in time, whereas for the time-varying forcing simulations, one turbulence measure is chosen to remain fixed in time. Varying the forcing coefficient in time allows us to maintain desired values for the TKE (k), the TKE dissipation rate (ϵ_k), or the vertical component of TKE (k_w). This approach builds on Ref. [26] which has been modified to incorporate buoyancy effects and derive a separate strategy for controlling k_w ; further details are provided in Appendix B. We find that the simulations with k or ϵ_k fixed in time traverse the solution space of Re_L and Fr_k differently from the simulations with constant forcing rate or fixed k_w . We illustrate this point in Fig. 1(a), where temporal trajectories of four simulations (C2, K3, D12, V6 in Table II) are plotted in the Re_L - Fr_k space. Re_L is on the x axis, and Fr_k is on the y axis. The diagonal dashed lines represent lines of constant Re_b , increasing in order of magnitude from 1 to 10^4 , plotted using $Re_b = Re_L Fr_k^2$. The constant- k simulation's trajectory (orange diamonds) falls on a line with a -1 slope. In contrast the constant- ϵ_k simulation's trajectory (blue stars) exhibits a $-1/2$ slope and maintains a constant value of Re_b at every instant in time. Finally, the remaining two types of simulations (constant forcing rate A and constant k_w ; red squares and black triangles) have trajectories without distinct slopes. In Fig. 1(b), which has the same axes as Fig. 1(a), we now plot the volume- and time-averaged values of Re_L and Fr_k for all simulations in Table II. For

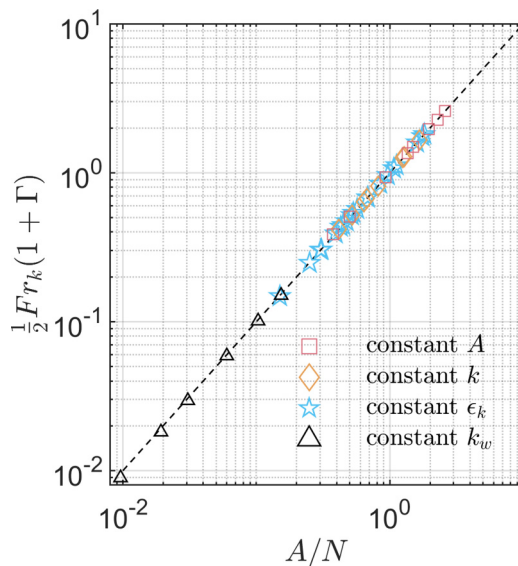


FIG. 2. Forcing input parameter (A/N) plotted versus the right-hand side of Eq. (12) for the steady-state, volume- and time-averaged energy balance for our simplified system. Given that the points for all four forcing strategies lie on the “one-to-one” line, it appears that all four strategies are well-described by the steady-state balance described in Eq. (12).

simulations with $Fr_k > 1$, $Re_L \approx 100$, and for simulations with $Fr_k < 1$, we note that Re_b decreases from about 100 to 10 with increasing stratification, indicating that a wider range of anisotropic scales are simulated at the expense of isotropic scales.

In the remainder of our paper, we discuss the flow dynamics under statistically stationary conditions. Therefore, we need to establish that our collective statistically stationary results are insensitive to which of the four temporal forcing strategies was used. We combine Eqs. (5) and (6) under statistically stationary conditions and divide by N to arrive at

$$\frac{A}{N} = \frac{1}{2} Fr_k (1 + \Gamma). \quad (12)$$

Equation (12) is one particular manifestation of the nondimensional total energy budget, and it also relates the input parameter A/N to two output parameters Fr_k and Γ . For $\Gamma \ll 1$, Eq. (12) can be simplified to $A/N \approx \frac{1}{2} Fr_k$, which provides a way to estimate the expected value of Fr_k for a given value of A/N . We plot the two sides of (12) as the x and y axes, respectively, in Fig. 2. Each symbol represents the two sides of Eq. (12) after volume and time averaging, and each color and symbol combination corresponds to one of the four temporal forcing strategies. Given that the points for all four forcing strategies lie on the “one-to-one” line, it appears that all four strategies are well-described by the steady-state balance described in Eq. (12). Based on this empirical observation, we do not indicate the forcing strategy in our subsequent figures (this also allows for greater visual simplicity).

B. Characterization of turbulence anisotropy

As the degree of stable stratification increases relative to the momentum forcing (larger N relative to A), the turbulence becomes increasingly anisotropic due to the enhanced damping of vertical velocity fluctuations. We quantify this effect in Fig. 3(a) by plotting the mean-squared horizontal and vertical velocity fluctuations versus the turbulent Froude number. The overbars denote volume and time averaging, and both squared velocity components have been normalized

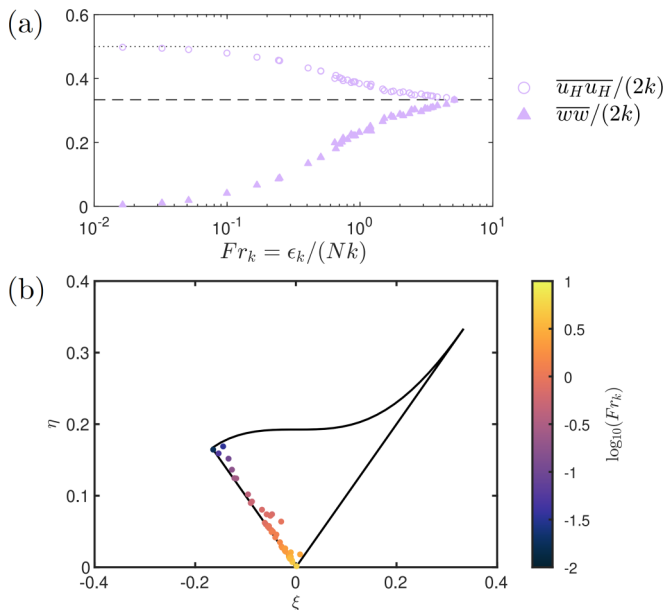


FIG. 3. (a) Normalized mean-squared horizontal velocity fluctuations (circles) and mean-squared vertical velocity fluctuations (triangles) versus turbulent Froude number. (b) Lumley triangle visualization of simulations colored by turbulent Froude number. In panel (a), the horizontal dashed line corresponds to the value of $1/3$, which is expected of isotropic turbulence, and the horizontal dotted line corresponds to the value of $1/2$, which is expected of two-component, disklike turbulence. In panel (b), stronger stratification (smaller turbulent Froude number) corresponds to increasingly anisotropic turbulence, corresponding to the movement from the isotropic corner of the Lumley triangle ($\xi = 0, \eta = 0$) to the two-component, disklike turbulence limit in the upper left.

by twice the TKE. Also, the horizontal velocity fluctuations have been calculated by averaging the x - and y -velocity components together, leveraging the axisymmetry of our simulations about the z axis. At large turbulent Froude numbers (weaker stratification relative to momentum forcing), the normalized squared velocities approach a value of $1/3$ (marked by the horizontal dashed line), which is the limiting behavior for isotropic turbulence. As the turbulent Froude number decreases (stronger stratification relative to momentum forcing), the normalized squared vertical velocities (triangles) monotonically decrease to 0, while the normalized squared horizontal velocities (circles) monotonically increase to a value of $1/2$ (marked by the horizontal dotted line), which is the limiting behavior for two-dimensional, axisymmetric turbulence.

We further characterize the flow anisotropy through the Lumley triangle visualization in Fig. 3(b). The x - and y -coordinate variables ξ and η are related to the second and third invariants of the Reynolds stress tensor, which can also be expressed in terms of the eigenvalues of the Reynolds stress tensor [23,27]. Following Ref. [28], we briefly discuss some notable aspects of the Lumley triangle. The bottom-most corner represents the isotropic limit, where all three diagonal Reynolds stress components are equally important. The left corner represents the two-component, disklike turbulence limit, where two diagonal components of the Reynolds stress tensor are equally important. The right corner represents the one-component, rodlike turbulence limit where only a single diagonal component of the Reynolds stress tensor is important. The top curve connects the two-component, disklike and one-component, rodlike limits, and the area within the Lumley triangle represents all possible turbulent states. When calculating ξ and η , we have used the volume- and time-averaged Reynolds stress tensor, but unlike for Fig. 3(a), we have not averaged the two horizontal Reynolds stress components. From Fig. 3(b), we can see that our simulations lie close

to the disklike turbulence leg, indicating that axisymmetric conditions are well satisfied for the majority of our simulations. With decreasing turbulent Froude number (indicated by color), our simulations move from the isotropic limit at the origin ($\xi = 0, \eta = 0$) to the two-component, disklike turbulence limit at the left corner. This suggests that our set of simulations span the entire physical or realizable range of axisymmetric, stably stratified turbulence described by our governing equations.

Before proceeding to the presentation of the volume-averaged budgets, we wish to broadly compare the physical-space, linear forcing used in this study and the spectral-space, vortical forcing which has been commonly used in previous studies of homogeneous stably stratified turbulence (e.g., Refs. [18,29–33]). We see these two forcing strategies as differing in three key ways: (i) whether energy is directly injected into the vertical component of TKE; (ii) whether forcing is restricted to a narrow band of large wave numbers; and (iii) whether forcing is restricted to vertically homogeneous modes ($k_z = 0$).

First, vortical forcing introduces additional large-scale anisotropy compared to linear forcing since it is only active in the horizontal momentum equations. Therefore, even for weak stratification ($\text{Fr}_k \gg 1$), vortical forcing requires nonzero pressure-strain correlations to drive vertical velocity fluctuations for 3D turbulence. For vortical forcing, this implies anisotropic, diagonal Reynolds stresses even in the limit of no stratification. As stratification is increased, we observe that linear forcing naturally becomes anisotropic due to the competing effects of forcing and buoyancy ($k_H > k_w$), and for very strong stratification strengths ($\text{Fr}_k \ll 1$), k_w (and therefore the direct injection of k_w by linear forcing, $2Ak_w$) becomes negligible. As a result, like in vortical forcing simulations, we expect the vertical flow dynamics from our linear forcing simulations to become more emergent (i.e., less dictated by the details of the forcing) for $\text{Fr}_k \ll 1$. With regards to Figs. 3(a) and 3(b), we expect vortically forced stratified turbulence to have normalized squared horizontal and vertical velocity fluctuations that are larger and smaller, respectively, compared to the HIT limit of $1/3$ (horizontal dashed line), and we expect it to not reach the isotropic limit at the origin but rather occupy $\eta > 0$ along the disklike turbulence leg of the Lumley triangle.

Second, vortical forcing injects energy in a narrow band of wave numbers, whereas physical-space linear forcing injects energy at all wave numbers. For isotropic turbulence simulations, using band-limited forcing leads to large-eddy scales that are twice as large compared to physical-space forcing (see Fig. 9 of Ref. [22] and also Ref. [34]). Therefore, for $\text{Fr}_k \gg 1$ where buoyancy effects are negligible, we speculate that vortical forcing could lead to larger Reynolds numbers compared to physical-space linear forcing. For $\text{Fr}_k \lesssim 1$, however, we are less certain about how the forcing bandwidth will interact with the anisotropic large scales. Third, vortical forcing restricts energy injection to vertically homogeneous modes ($k_z = 0$), whereas physical-space linear forcing does not. We suspect that this distinction will also lead to notable differences for all values of Fr_k between vortical and linear forcing. We believe that a quantitative comparison of vortical and linear forcing across a wide range of stratification strengths would be instructive in a future study.

C. TKE and TPE budgets

We now turn to the steady-state, volume- and time-averaged TKE and TPE budgets [Eqs. (5) and (6)] as a function of the turbulent Froude number [Figs. 4(a) and 4(b)]. In both figures, each of the terms in the budget have been normalized by their respective production terms such that all terms are bounded between ± 1 , and to match Eqs. (5) and (6), the normalized TKE and TPE dissipation rates and buoyancy flux are plotted with minus signs. In Fig. 4(a) [related to Eq. (5)], the normalized production accounts for all TKE generation (black triangles) regardless of Fr_k , while the sum of the normalized buoyancy flux (orange stars) and TKE dissipation rate (red triangles) account for the total loss of TKE. In Fig. 4(b) [related to Eq. (6)], the normalized buoyancy flux accounts for all TPE generation (orange triangles), and the normalized TPE dissipation rate accounts for the total loss of TPE (red triangles). The normalized residuals (gray squares) for each budget are close to zero, indicating that our simulations have reached statistically steady-state conditions.

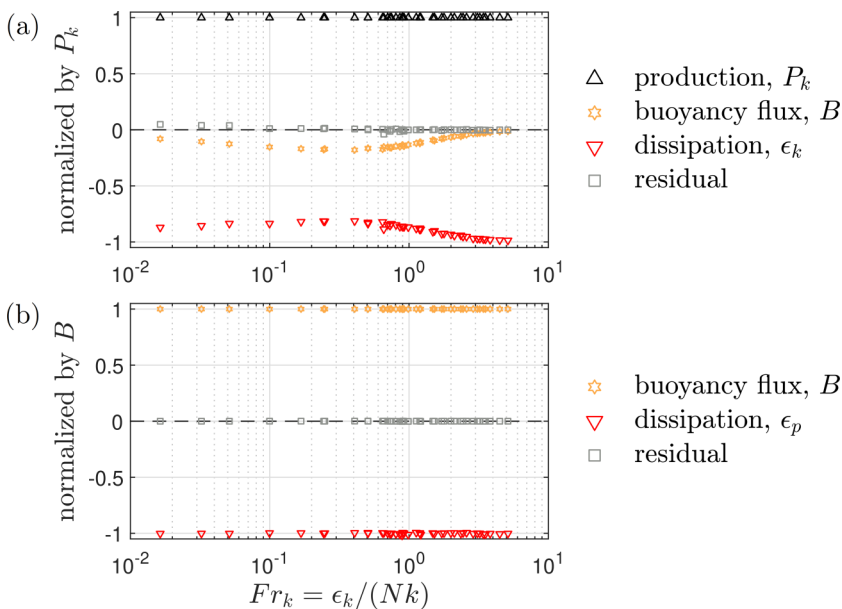


FIG. 4. Steady-state, volume- and time-averaged budgets of (a) TKE and (b) TPE as a function of the turbulent Froude number. The two panels correspond to Eqs. (5) and (6), respectively.

D. Horizontal and vertical TKE budgets

Previous works have characterized the anisotropy of stably stratified turbulence by separately considering the horizontal and vertical spectra of TKE and TPE, which exhibit different wave number scaling laws for scales larger than the Ozmidov scale (e.g., Refs. [30,31,33,35]). Here, we have separated TKE into its horizontal and vertical components to further illustrate the effects of turbulence anisotropy on the energetics. This decomposition retains the pressure-strain correlations, which sum to zero for incompressible flow. By studying their respective steady-state, volume- and time-averaged budgets [Eqs. (9) and (10)] in Figs. 5(a) and 5(b), we demonstrate that the pressure-strain correlations along with the buoyancy flux significantly affects the energy exchange of scales larger than the Ozmidov scale for stably stratified turbulence. As before, we normalize all terms in each budget by the sum of their respective production terms to keep all terms normalized between ± 1 , and to match Eqs. (9) and (10), the normalized dissipation rates of k_H and k_w and the buoyancy flux are plotted with minus signs.

We first consider the budget of the horizontal component of TKE [Fig. 5(a)]. At high Froude numbers, the pressure-strain correlation is negligible (blue x's), and direct production (black triangles) and dissipation (red triangles) are in balance. As the stratification increases, the pressure-strain correlation acts as a sink of horizontal TKE as seen by the reduction in the dissipation term. There is a region between $Fr_k \approx 0.7$ and $Fr_k \approx 0.2$ where the balance is fairly constant, but for $Fr_k < 0.2$, the pressure-strain correlation weakens as a sink of horizontal TKE and the dissipation rate grows in relative importance as a sink of horizontal TKE.

We next consider the budget of the vertical component of TKE [Fig. 5(b)]. At high Froude numbers, both the pressure-strain correlation (blue x's) and buoyancy flux (orange stars) are negligible, and production (black triangles) and dissipation (red triangles) are in balance. As the stratification increases in magnitude, the vertical pressure-strain correlation term also increases in relative importance as a source of k_w to the point where at $Fr_k \approx 0.7$, direct production and pressure-strain correlation contribute equally to the generation of k_w . For $Fr_k < 0.7$ direct production diminishes, eventually becoming negligible at small Fr_k , so that k_w depends entirely on the pressure-strain correlation to “stay alive.” The buoyancy flux monotonically decreases with decreasing turbulent

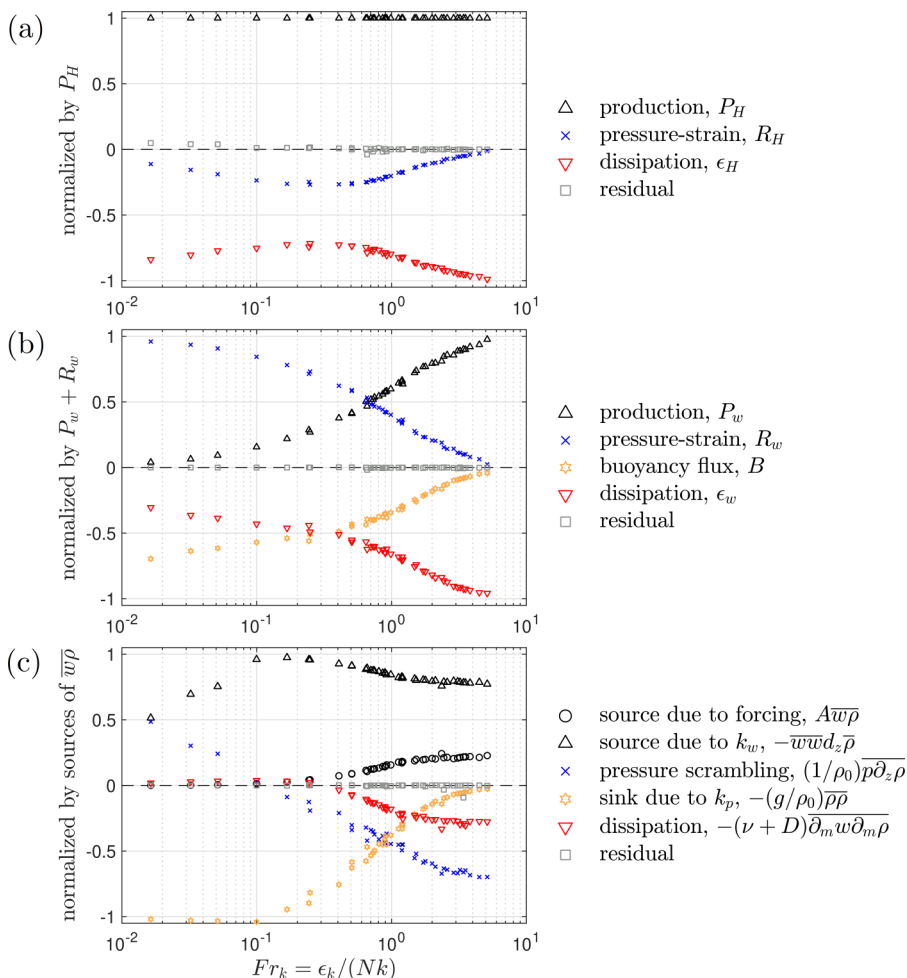


FIG. 5. Steady-state, volume- and time-averaged budgets of (a) k_H , (b) k_w , and (c) $\overline{w\rho}$ as a function of the turbulent Froude number. The three panels correspond to Eqs. (9), (10), and (11), respectively.

Froude number, but there is a change in slope around $\text{Fr}_k \approx 0.7$, at which point the dissipation rate becomes a weaker sink of k_w with decreasing Fr_k .

E. Vertical density flux budget

Now, we consider the steady-state, volume- and time-averaged budget of the vertical density flux as a function of the turbulent Froude number [Fig. 5(c)]. As before, for each turbulent Froude number, every term has been normalized by the sum of all source terms to keep all normalized terms between ± 1 . At high turbulent Froude numbers, the sink due to k_p (orange stars) is negligible, and there is a balance among the remaining four terms. As the stratification magnitude increases (until $\text{Fr}_k \approx 0.1$), the source due to forcing (black circles), pressure scrambling (blue x's), and dissipation (red triangles) all approach 0, while the source due to k_w (black triangles) and sink due to k_p grow in relative importance until they are balancing each other. As stratification increases further ($\text{Fr}_k < 0.1$), the source due to k_w decreases in relative importance, and the pressure scrambling term switches signs and becomes an equally important source of the vertical density flux for our smallest turbulent Froude number simulation. The sink due to k_p remains the single dominant loss term for $\text{Fr}_k < 0.1$.

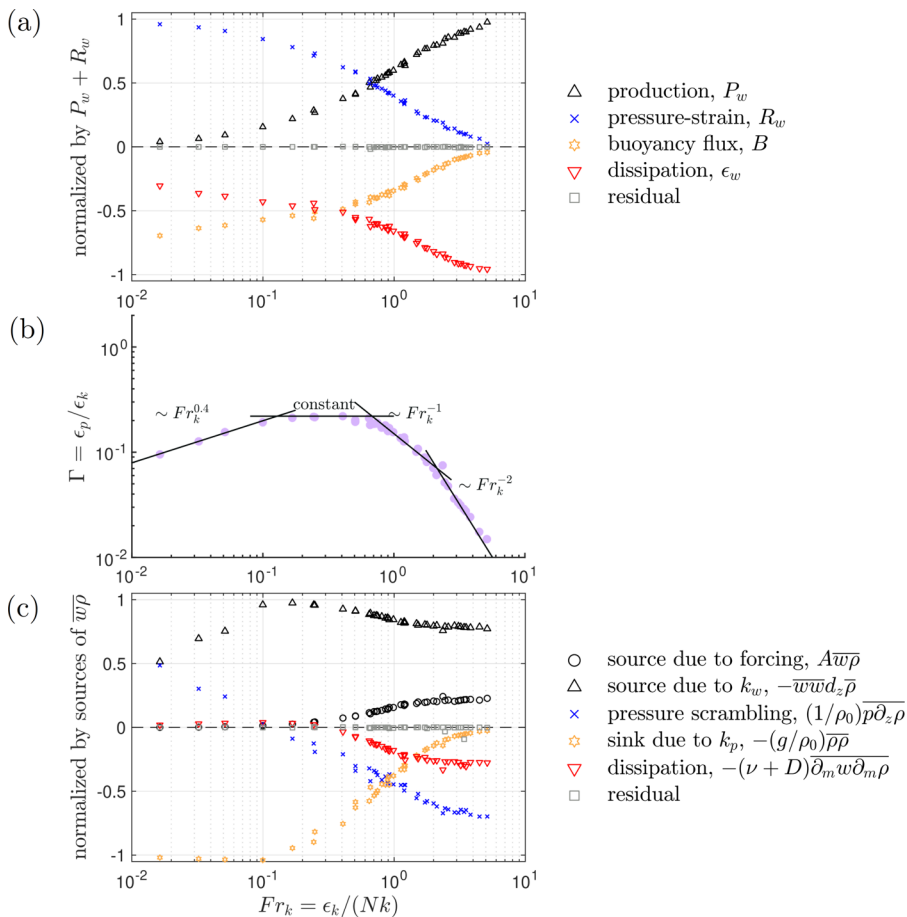


FIG. 6. (b) Volume- and time-averaged values of Γ versus Fr_k . Figures 5(b) and 5(c) are reproduced in panels (a) and (c) for convenience. The simulations exhibit four mixing regimes with the power-law slopes of Γ changing at $Fr_k \approx 0.1, 0.7$, and 2.1 . The low Froude number slope of $\Gamma \sim Fr_k^{0.4}$ is an empirical fit and remains an open question in the literature.

F. Mixing coefficient versus turbulent Froude number

Finally, we consider the behavior of the mixing coefficient Γ as a function of the turbulent Froude number [Fig. 6(b)]. For the highest turbulent Froude numbers, the mixing coefficient exhibits a -2 slope dependence. This changes to a -1 slope dependence at $Fr_k \approx 2.1$, and then to no dependence at $Fr_k \approx 0.7$. These slopes all agree with the predictions from the analysis of Ref. [17]. Furthermore, for $Fr_k < 0.2$, our simulations have mixing coefficient values that decrease (an $Fr_k^{0.4}$ dependence), which qualitatively agrees with the findings of Ref. [18], which also reported decreasing values of Γ for small values of Fr_k . Intriguingly, while the exact values of Fr_k at which these transitions occur are most likely not universal across all types of stably stratified turbulent flows (e.g., Ref. [36]), we wish to emphasize here that these transition points coincide with specific transitions in the normalized budgets of k_w and $\bar{w}\rho$ described in Figs. 5(b) and 5(c). For easier visualization, we have reproduced these two budgets as Figs. 6(a) and 6(c), respectively. There are three notable observations we make in this regard. First, the transition from $\Gamma \sim Fr_k^{-1}$ to $\Gamma \sim Fr_k^0$ at $Fr_k \approx 0.7$ coincides with the point at which the pressure-strain and production terms equally generate k_w . Second, the extent of the $\Gamma \sim Fr_k^0$ region ($0.2 < Fr_k < 0.7$) also matches the plateau in the normalized pressure-strain

correlation in the horizontal TKE budget [Fig. 5(a)]. Finally, the transition from $\Gamma \sim \text{Fr}_k^0$ to $\Gamma \sim \text{Fr}_k^{0.4}$ at $\text{Fr}_k \approx 0.1$ coincides with when the pressure scrambling term switches sign to become a source of vertical density flux, and where the sink due to TPE reaches a maximum.

G. An alternative expression for the mixing efficiency and comments on Reynolds number effects

Up to this point, we have presented our results solely in terms of Fr_k , but our simulations also exhibit variations in Re_L (and Re_b). While the primary variations of our quantities of interest have been captured by Fr_k , we expect our results to be modified by increasing Reynolds number. For weak stratification ($\text{Fr}_k \approx 3$), Ref. [18] showed that Γ decreases as the Taylor-microscale Reynolds number ($\text{Re}_\lambda \sim \text{Re}_L^{1/2}$) is increased. Here, we attempt to extend their finding to all stratification strengths by considering an alternative definition of the mixing efficiency.

Following Ref. [37], we manipulate the steady-state, time- and volume-averaged k_w budget to arrive at an alternative expression for the mixing efficiency

$$\text{Ri}_f = \frac{1}{1 - c_3} \left[\frac{R_w}{P_k} + b_{33} - c_3 + \frac{1}{3} \right], \quad (13)$$

where $c_3 = \epsilon_w/\epsilon_k$ is the fraction of the TKE dissipation rate that is accounted for by the dissipation rate of k_w ; R_w is the pressure-strain correlation term in the k_w budget; $P_k = 2Ak$ is the TKE production rate; and b_{33} is the third diagonal entry of the normalized Reynolds anisotropy tensor $b_{ij} = \overline{u_i u_j} / (2k) - (1/3)\delta_{ij}$. To arrive at Eq. (13), we have used Eq. (6) to replace B with ϵ_p in Eq. (10) and divided by the total production of TKE, P_k . Then, using $P_k = \epsilon_k + \epsilon_p$, which comes from combining Eqs. (5) and (6), and letting $\epsilon_w = c_3\epsilon_k$, we have rewritten the term involving ϵ_w and solved for the mixing efficiency Ri_f .

For large Reynolds numbers (either $\text{Re}_L \gg 1$ for $A/N \gtrsim 1$ or $\text{Re}_b \gg 1$ for $A/N \lesssim 1$), we expect $c_3 \rightarrow 1/3$ based on arguments about the local isotropy of dissipative scales (e.g., Refs. [20,38]). Under this limit, Eq. (13) becomes

$$\lim_{\text{Re} \gg 1} \text{Ri}_f = \frac{3}{2} \left[\frac{R_w}{P_k} + b_{33} \right]. \quad (14)$$

Then, Eq. (14) establishes a direct link between how efficiently the density field is irreversibly mixed to the degree of large-scale anisotropy as quantified by R_w/P_k and b_{33} . For negligible stratification, $b_{33} \rightarrow 0$ corresponding to the isotropic turbulence limit, and empirically from Fig. 5(b), we expect $R_w/P_k \rightarrow 0$. This leads to $\text{Ri}_f \rightarrow 0$, which agrees with the physical picture where there is no background density gradient to mix. For very strong stratification, $b_{33} \rightarrow -1/3$ corresponding to the two-component, disklike turbulence limit (see Fig. 3). Since Ri_f is a positive semidefinite quantity, this requires $R_w/P_k \geq -b_{33} = 1/3$. Due to lack of further constraints on R_w/P_k at large Reynolds numbers, we are unable to determine whether Ri_f remains finite using Eq. (14) in the limit of very strong stratification. In this limit, Ref. [18] finds $\Gamma \approx 0.33$ ($\text{Ri}_f \approx 0.25$), yet this simulation is characterized by $\text{Re}_b \approx 17$, indicating that Ri_f would likely still be dependent on Re_b .

Because Fr_k and Re vary simultaneously for our simulations, we are unable to demonstrate whether R_w/P_k , b_{33} , and c_3 depend primarily on Fr_k , Re , or both. Nevertheless, we plot R_w/P_k and b_{33} as a function of Fr_k in Figs. 7(a) and 7(b) with Re shown in color, and we plot c_3 as a function of Re in Fig. 7(c) with Fr_k shown in color. Here, we have defined the Reynolds number as $\text{Re} = \text{Re}_b$ for $A/N < 1/2$ and $\text{Re} = \text{Re}_L$ for $A/N \geq 1/2$ guided by Eq. (14). For $\text{Fr}_k > 1$, $\text{Re} \approx 100$ [see also Fig. 1(b)], therefore, the variations of R_w/P_k and b_{33} from our simulations are primarily due to Fr_k (this does not, however, rule out Re effects on R_w/P_k and b_{33} for $\text{Fr}_k > 1$ more broadly). For $\text{Fr}_k < 1$, Re approximately varies from 10 to 100, indicating that R_w/P_k and b_{33} from our simulations are varying due to both Fr_k and Re . In Fig. 7(c), we see that c_3 from our simulations decreases from approximately $1/3$ towards 0 with decreasing Re , but once again due to simultaneous variations of Re and Fr_k , we are unable to test whether c_3 depends solely on Re from our simulations alone. We

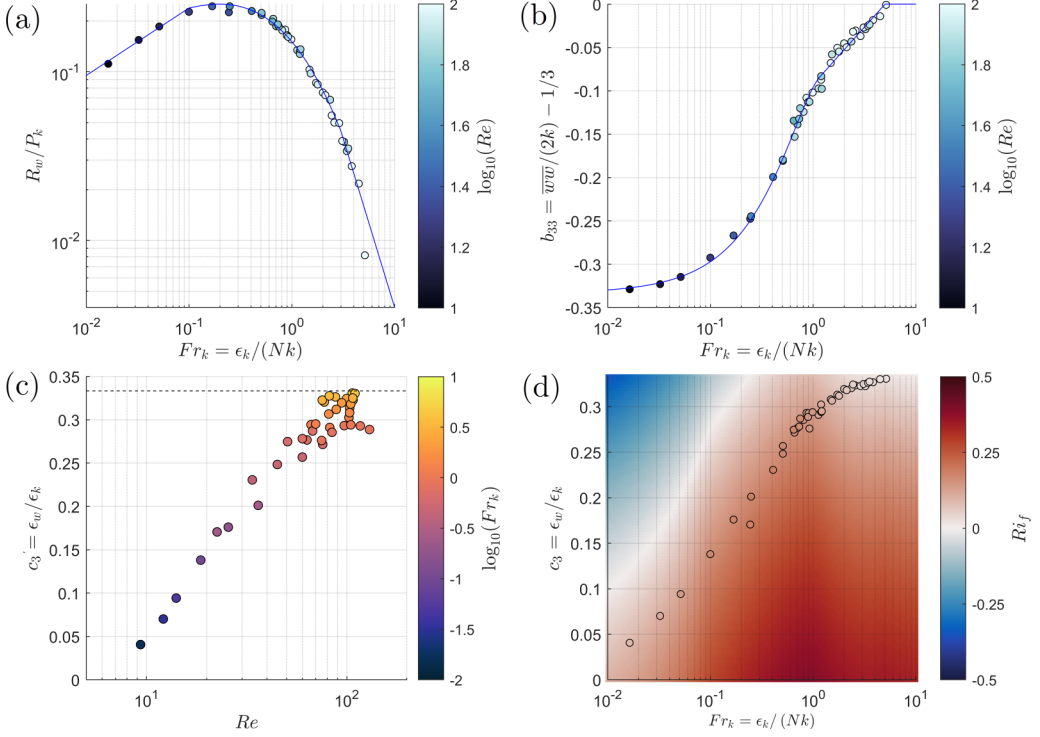


FIG. 7. (a) R_w/P_k and (b) b_{33} plotted as a function of Fr_k with the magnitude of Re shown in color and the least-squares fits to the DNS values shown by thin blue lines. (c) $c_3 = \epsilon_w/\epsilon_k$ plotted as a function of Re with the magnitude of Fr_k shown in color and the dashed horizontal line marking the value of $c_3 = 1/3$, which is expected under local isotropy of dissipative scales. (d) Contour plot of Ri_f as a function of Fr_k and c_3 where (13) is evaluated for each Fr_k by using the least-squares fits of R_w/P_k and b_{33} shown in panels (a) and (b) and varying c_3 . Colored circles represent the actual values of Ri_f from DNS.

hope to disentangle the Fr_k and Re effects in a future study by systematically increasing Re over a large range of Fr_k .

With these limitations in mind, we proceed to explore Eq. (13) by making two simplifying assumptions. First, we assume that R_w/P_k and b_{33} depend only on Fr_k , and second, we assume that c_3 depends solely on Re . By separately accounting for the effects of anisotropic scales (through R_w/P_k and b_{33}) and isotropic scales (through c_3), we are assuming that the anisotropic and isotropic scales interact negligibly with one another. This allows us to take the values of R_w/P_k and b_{33} at each value of Fr_k from our simulations and evaluate Eq. (13) to explore how Ri_f varies for $c_3 \in [0, 1/3]$. We do this with full acknowledgment that our two assumptions correspond to a physically incorrect picture that disagrees with theoretical scalings of strongly stratified turbulence of Ref. [39] and empirical observations of thin, layered structures, indicating the interaction of large horizontal scales with small vertical scales (e.g., Refs. [30,31,35,36,40,41]).

With this caveat in mind, we plot the estimated values of Ri_f from Eq. (13) (colored contours) and the actual Ri_f values from our simulations (colored circles) in Fig. 7(d) with Fr_k on the x axis and c_3 on the y axis. To create the colored contour plot from Eq. (13), we have used least-squares fits of R_w/P_k and b_{33} as a function of Fr_k shown by thin blue lines in Figs. 7(a) and 7(b). The least-squares fit of R_w/P_k included three parts: $R_w/P_k \approx a_1 Fr_k^{0.4}$ for $Fr_k \leq 10^{-1}$; $\log(R_w/P_k) \approx a_2 \log(Fr_k)^3 + b_2 \log(Fr_k)^2 + c_2 \log(Fr_k) + d_2$ for $10^{-1} \leq Fr_k \leq 3$; $R_w/P_k \approx a_3 Fr_k^{-2}$ for $Fr_k \geq 3$. The functional forms, coefficients $a_1 = 0.6$ and $a_3 = 0.4$, and the boundary values

of Fr_k for the three parts were chosen empirically; however, the coefficients a_2 , b_2 , c_2 , and d_2 were found through a least-squares fitting process that ensured piecewise continuity of the three parts. The least-squares fit of b_{33} also included three parts: $b_{33} \approx a_4 Fr_k^2 + b_4 Fr_k + c_4$ for $Fr_k \leq 1.2$; $b_{33} \approx a_5 \log(Fr_k) + b_5$ for $1.2 \leq Fr_k \leq 5$; $b_{33} \approx a_6$ for $Fr_k \geq 5$. Once again, the functional forms and the boundary values of Fr_k for the three parts were chosen empirically, but the values for $c_4 = -1/3$ and $a_6 = 0$ were constrained theoretically based on the limiting values of b_{33} for small and large Fr_k , respectively. As before, the remaining coefficients (a_4 , b_4 , a_5 , and b_5) were found through a least-squares fitting process that ensured piecewise continuity of the three parts. Positive values of Ri_f are indicated in red, and negative values are indicated in blue.

First, we note that the positive semidefinite property of Ri_f is violated when we evaluate Eq. (13) with our two simplifying assumptions as indicated by the blue regions. We interpret this as a direct consequence of our unphysical assumptions. Second, at all values of Fr_k , we note that Ri_f decreases with increasing c_3 , which we are using as a proxy for increasing Re . This qualitatively agrees with the findings of Ref. [18] for weakly stratified turbulence, but more broadly, this seems to suggest that this inverse relationship between Ri_f and c_3 might hold true even for moderately and strongly stratified turbulence. In the limit of strongly stratified turbulence, our analysis agrees with the findings of Ref. [42], who explored the relationship between Ri_f and Re_b . As Ref. [42] varied Re_b from 1 to 10 for $Fr_k \approx 10^{-2}$, they observed a maximum value of Ri_f at $Re_b \approx 4$, which then decreased monotonically for increasing Re_b . In summary, we note that all RHS parameters in Eq. (13) depend both on Fr_k and Re , and this warrants a more thorough exploration of the relationship between Ri_f and Re , especially for the moderately and strongly stratified regimes.

IV. CONCLUSIONS

We have studied statistically stationary, axisymmetric, stably stratified turbulence under linear forcing. Our simulations spanned the complete range of axisymmetric turbulent states (that is realizable) from a combination of linear forcing and stable stratification, as demonstrated by the Lumley triangle visualization in Fig. 3(b). We found a number of notable results. First, as we increased stratification, the horizontal component of TKE increased monotonically, whereas the vertical component of TKE in our simulations decreased monotonically. Second, we highlighted the critical role that the pressure-strain correlations play in maintaining finite values of the vertical component of TKE with increasing stratification. Third, we have taken quantitative steps towards understanding what sets the mixing efficiency of stably stratified turbulence by connecting the shape of the mixing coefficient curve to the underlying dynamics and energetics of our model problem. As seen in Fig. 6, we connected the variations of the mixing coefficient with the turbulent Froude number to notable shifts in the energy budgets. Specifically, the turbulent Froude number where direct production and pressure-strain correlation equally contribute to the generation of the vertical component of TKE corresponds to the point where the mixing coefficient curve flattens out. Furthermore, the trend of the mixing coefficient decreasing from its peak value for even stronger stratification (smaller Fr_k) is also connected with a sign change of the pressure scrambling term in the vertical density flux budget. Finally, using an alternative expression for the mixing efficiency, we hypothesized that the mixing efficiency is likely to decrease with increasing Reynolds number for all turbulent Froude numbers. Unlike the universal scaling behaviors proposed by Ref. [17], we expect that conducting similar analyses for sheared, stably stratified turbulence will reveal important differences between them and the axisymmetric, stably stratified turbulence studied here, ultimately leading to a more nuanced and physically rich understanding of turbulent mixing associated with different types of stably stratified flows.

ACKNOWLEDGMENTS

Y.R.Y. gratefully acknowledges support from the Charles H. Leavell Fellowship of the Department of Civil and Environmental Engineering at Stanford University. We thank Drs. M. Bassenne,

P. Johnson, and J. Urzay for helpful discussions about linear forcing in the context of homogeneous, isotropic turbulence, and Y.R.Y. thanks M.-Y. Tsang for helpful comments regarding figure design.

APPENDIX A: REGARDING INITIALIZATION AND TEMPORAL AVERAGING

We have initialized most (30 of 42) of our velocity fields using divergence-free, isotropic fields generated based on a model spectrum from Ref. [43]. The exact form of the spectrum with dimensional coefficients follows from Eq. (3) of Ref. [26] and is given as

$$E_0(\kappa) = \frac{32k_0}{\kappa_0} \sqrt{\frac{2}{\pi}} \left(\frac{\kappa}{\kappa_0}\right)^4 \exp\left[-2\left(\frac{\kappa}{\kappa_0}\right)^2\right], \quad (\text{A1})$$

where $E_0(\kappa)$ is the three-dimensional model spectrum, k_0 is the initial turbulent kinetic energy, and κ_0 is the wave number at which the energy spectrum has its maximum. We used dimensional coefficient values of $k_0 = 2.75 \text{ m}^2/\text{s}^2$ and $\kappa_0 = 10 \text{ m}^{-1}$. We chose to initialize the density fluctuations by multiplying the vertical velocity fluctuations by a uniform factor c of either 0.1 or 0.2 [i.e., $\rho(\vec{x}, t = 0) = cw(\vec{x}, t = 0)$]. Unlike initializing with zero density fluctuations, our choice results in nonzero buoyancy fluxes from the start of the simulations.

The rest (12 of 42) of our simulations were initialized from statistically stationary velocity and density fields either from simulations C8 or D8 (see Table II). This choice significantly reduced the simulation spin-up time associated with the initial transient decay and growth that occur as the nonlinear terms become increasingly active. Because we time advance all simulations until flow statistics become statistically stationary, we expect our initialization choices to have negligible effects on the final flow states that are reached. We validate this assumption through our analysis of various budgets using the entire collection of simulations (e.g., Figs. 2, 4, and 5). In the final two columns of Table II, S denotes velocity fluctuations initialized using the model spectrum in Eq. (A1), and C8 or D8 indicates the simulations that were initialized using 3D snapshots from the statistically stationary portions of simulations C8 or D8.

For temporal averaging, we needed to define a window over which we could assume that the turbulence fluctuations were statistically stationary. Using the result shown in Fig. 3(b) of Ref. [33], we defined the start of the temporal averaging window as the first occurrence of $(\epsilon_k + \epsilon_p)/P_k > 1$ after the initial decay period. Physically, when our flow fields become statistically stationary, the volume-averaged TKE and TPE budgets can be simplified to $P_k \approx \epsilon_k + \epsilon_p$, where P_k is the TKE production rate, ϵ_k is the TKE dissipation rate, and ϵ_p is the TPE dissipation rate. Although the simulations with time-varying A did not exhibit the same marked initial decay of $(\epsilon_k + \epsilon_p)/P_k$ as the cases with constant A [see Fig. 8(a)], the same algorithm was used to determine the temporal averaging window for all sets of simulations except for the constant- k_w simulations. To illustrate this procedure, representative time series of $(\epsilon_k + \epsilon_p)/P_k$ and Γ from constant- A (red), constant- k (orange), and constant- ϵ_k (blue) simulations are shown in Fig. 8, where the x axis is time normalized by the buoyancy period $t_B = 2\pi/N$. This algorithm is well-behaved for all but simulations D4 and V1–V6, for which we manually selected $t/t_B \approx 1.3, 17.5, 8.8, 8.8, 5, 5,$ and 2.5 , respectively, as the beginning of our temporal averaging windows. These values were chosen visually based on the time series of Γ . The bounds of the temporal averaging windows are provided in the columns labeled t_s/t_B and t_f/t_B in Table II.

APPENDIX B: DERIVATION OF TIME-VARYING CONTROLLERS AND DISCUSSION ABOUT CONTROL PARAMETERS

The subsequent derivations closely follow those provided in Ref. [26] with minor modifications to incorporate buoyancy effects.

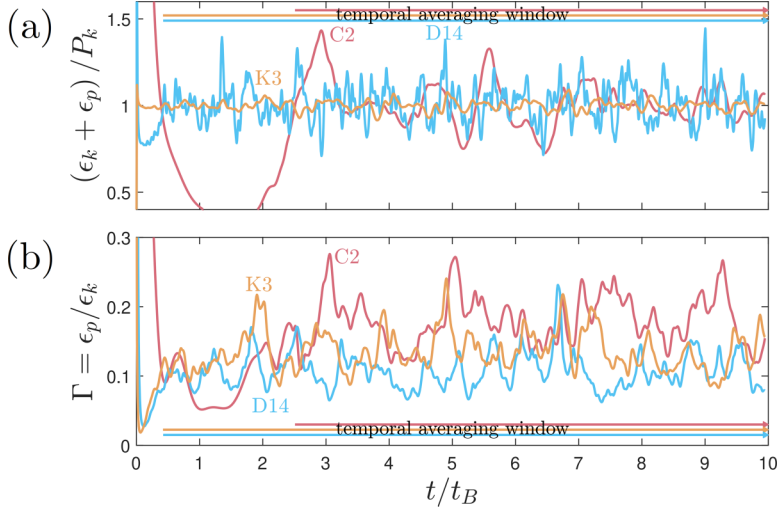


FIG. 8. Time series of volume-averaged (a) $(\epsilon_k + \epsilon_p)/P_k$ and (b) Γ from simulations C2 (red), K3 (orange), and D14 (blue). Temporal averaging windows are marked by horizontal lines. Note the marked decay and growth of $(\epsilon_k + \epsilon_p)/P_k$ for the constant- A simulation (red) in contrast to the behavior of the constant- k and constant- ϵ_k simulations (orange and blue, respectively).

First, we consider the volume-averaged TKE budget (5), which is reproduced here:

$$\frac{dk}{dt} = 2Ak - \frac{g}{\rho_0} \overline{w\rho} - \nu \overline{\frac{\partial u_j}{\partial x_m} \frac{\partial u_j}{\partial x_m}} = 2Ak - B - \epsilon_k. \quad (\text{B1})$$

Then, we choose A as

$$A(t) = \frac{\epsilon_k(t) + B(t) - \frac{G}{\tau_L}[k(t) - k_\infty]}{2k(t)}, \quad (\text{B2})$$

such that Eq. (B1) simplifies to

$$\frac{dk}{dt} = -\frac{G}{\tau_L}[k(t) - k_\infty], \quad (\text{B3})$$

where k_∞ is the target value of k , τ_L is a relaxation time scale, and G is a positive, nondimensional gain parameter. Note that τ_L/G now determines the typical time scale required for $k(t) \rightarrow k_\infty$.

Next, we differentiate Eq. (3) with respect to x_m and multiply by $2\nu\partial_m u_j$. Then, we volume average the equation, and using the fact that our flow statistics are homogeneous in all three directions, we arrive at

$$\frac{d\epsilon_k}{dt} = -2\nu \overline{\frac{\partial u_j}{\partial x_m} \frac{\partial u_l}{\partial x_m} \frac{\partial u_j}{\partial x_l}} - 2\nu^2 \overline{\frac{\partial^2 u_j}{\partial x_m \partial x_l} \frac{\partial^2 u_j}{\partial x_m \partial x_l}} + 2A\epsilon_k - \frac{2vg}{\rho_0} \overline{\frac{\partial w}{\partial x_m} \frac{\partial \rho}}. \quad (\text{B4})$$

Defining the first two terms of the right-hand side of Eq. (B4) as $-D_{\epsilon_k}$ and the fourth term as $-B_{\epsilon_k}$, we choose A as

$$A(t) = \frac{D_{\epsilon_k}(t) + B_{\epsilon_k}(t) - \frac{G}{\tau_L}[\epsilon_k(t) - \epsilon_{k,\infty}]}{2\epsilon_k(t)}, \quad (\text{B5})$$

such that Eq. (B4) simplifies to

$$\frac{d\epsilon_k}{dt} = -\frac{G}{\tau_L}[\epsilon_k(t) - \epsilon_{k,\infty}], \quad (\text{B6})$$

where $\epsilon_{k,\infty}$ is the target value of ϵ_k . Now, τ_L/G determines the typical time scale required for $\epsilon_k(t) \rightarrow \epsilon_{k,\infty}$.

Finally, we consider the volume-averaged budget of the vertical component of TKE (10), which is reproduced here:

$$\frac{dk_w}{dt} = 2Ak_w + \frac{1}{\rho_0} \overline{ps_{33}} - \frac{g}{\rho_0} \overline{\rho w} - \nu \overline{\frac{\partial w}{\partial x_m} \frac{\partial w}{\partial x_m}} = 2Ak_w + R_w - B - \epsilon_w. \quad (\text{B7})$$

Then, we choose A as

$$A(t) = \frac{\epsilon_w(t) + B(t) - R_w(t) - \frac{G}{\tau_L}[k_w(t) - k_{w,\infty}]}{2k_w(t)}, \quad (\text{B8})$$

such that Eq. (B7) simplifies to

$$\frac{dk_w}{dt} = -\frac{G}{\tau_L}[k_w(t) - k_{w,\infty}], \quad (\text{B9})$$

where $k_{w,\infty}$ is the target value of k_w . Here, τ_L/G determines the typical time scale required for $k_w(t) \rightarrow k_{w,\infty}$.

Following Ref. [26], for all simulations with $A(t)$, we used a gain parameter of $G = 67$ and a relaxation time scale of $\tau_L = 1$, except simulations K6 and K7, for which we used $\tau_L = 0.92$ and 2, respectively. The particular choice of τ_L and G are unimportant as long as the effective relaxation timescale τ_L/G is shorter than the physical timescales associated with the parameters of interest (k , ϵ_k , and k_w). This point is explored in greater detail for the constant- k and constant- ϵ_k controllers in Ref. [26].

-
- [1] C. Wunsch and R. Ferrari, Vertical mixing, energy, and the general circulation of the oceans, *Annu. Rev. Fluid Mech.* **36**, 281 (2004).
 - [2] W. D. Smyth, H. T. Pham, J. N. Moum, and S. Sarkar, Pulsating turbulence in a marginally unstable stratified shear flow, *J. Fluid Mech.* **822**, 327 (2017).
 - [3] A. Adcroft, W. Anderson, V. Balaji, C. Blanton, M. Bushuk, C. O. Dufour, J. P. Dunne, S. M. Griffies, R. Hallberg, M. J. Harrison, I. M. Held, M. F. Jansen, J. G. John, J. P. Krasting, A. R. Langenhorst, S. Legg, Z. Liang, C. McHugh, A. Radhakrishnan, B. G. Reichl *et al.*, The GFDL global ocean and sea ice model OM4.0: Model description and simulation features, *J. Adv. Model. Earth Syst.* **11**, 3167 (2019).
 - [4] C. de Lavergne, G. Madec, J. Le Sommer, A. J. G. Nurser, and A. C. Naveira Garabato, The impact of a variable mixing efficiency on the abyssal overturning, *J. Phys. Oceanogr.* **46**, 663 (2015).
 - [5] A. Mashayek, H. Salehipour, D. Bouffard, C. P. Caulfield, R. Ferrari, M. Nikurashin, W. R. Peltier, and W. D. Smyth, Efficiency of turbulent mixing in the abyssal ocean circulation, *Geophys. Res. Lett.* **44**, 6296 (2017).
 - [6] L. Cimoli, C. P. Caulfield, H. L. Johnson, D. P. Marshall, A. Mashayek, A. C. Naveira Garabato, and C. Vic, Sensitivity of deep ocean mixing to local internal tide breaking and mixing efficiency, *Geophys. Res. Lett.* **46**, 14622 (2019).
 - [7] T. R. Osborn, Estimates of the local rate of vertical diffusion from dissipation measurements, *J. Phys. Oceanogr.* **10**, 83 (1980).
 - [8] H. Salehipour and W. R. Peltier, Diapycnal diffusivity, turbulent Prandtl number and mixing efficiency in Boussinesq stratified turbulence, *J. Fluid Mech.* **775**, 464 (2015).
 - [9] S. K. Venayagamoorthy and J. R. Koseff, On the flux Richardson number in stably stratified turbulence, *J. Fluid Mech.* **798**, R1 (2016).
 - [10] G. N. Ivey and J. Imberger, On the nature of turbulence in a stratified fluid. Part I: The energetics of mixing, *J. Phys. Oceanogr.* **21**, 650 (1991).

- [11] A. F. Waterhouse, J. A. MacKinnon, J. D. Nash, M. H. Alford, E. Kunze, H. L. Simmons, K. L. Polzin, L. C. St. Laurent, O. M. Sun, R. Pinkel, L. D. Talley, C. B. Whalen, T. N. Huussen, G. S. Carter, I. Fer, S. Waterman, A. C. Naveira Garabato, T. B. Sanford, and C. M. Lee, Global patterns of diapycnal mixing from measurements of the turbulent dissipation rate, *J. Phys. Oceanogr.* **44**, 1854 (2014).
- [12] G. N. Ivey, K. B. Winters, and J. R. Koseff, Density stratification, turbulence, but how much mixing? *Annu. Rev. Fluid Mech.* **40**, 169 (2008).
- [13] M. C. Gregg, E. A. D'Asaro, J. J. Riley, and E. Kunze, Mixing efficiency in the ocean, *Annu. Rev. Mar. Sci.* **10**, 443 (2018).
- [14] C. P. Caulfield, Open questions in turbulent stratified mixing: Do we even know what we do not know? *Phys. Rev. Fluids* **5**, 110518 (2020).
- [15] C. P. Caulfield, Layering, instabilities, and mixing in turbulent stratified flows, *Annu. Rev. Fluid Mech.* **53**, 113 (2021).
- [16] S. G. Monismith, J. R. Koseff, and B. L. White, Mixing efficiency in the presence of stratification: When is it constant? *Geophys. Res. Lett.* **45**, 5627 (2018).
- [17] A. Garanaik and S. K. Venayagamoorthy, On the inference of the state of turbulence and mixing efficiency in stably stratified flows, *J. Fluid Mech.* **867**, 323 (2019).
- [18] A. Maffioli, G. Brethouwer, and E. Lindborg, Mixing efficiency in stratified turbulence, *J. Fluid Mech.* **794**, R3 (2016).
- [19] L. H. Shih, J. R. Koseff, G. N. Ivey, and J. H. Ferziger, Parameterization of turbulent fluxes and scales using homogeneous sheared stably stratified turbulence simulations, *J. Fluid Mech.* **525**, 193 (2005).
- [20] G. D. Portwood, S. M. de Bruyn Kops, and C. P. Caulfield, Asymptotic Dynamics of High Dynamic Range Stratified Turbulence, *Phys. Rev. Lett.* **122**, 194504 (2019).
- [21] T. S. Lundgren, Linearly forced isotropic turbulence, in *Annual Research Briefs* (Center for Turbulence Research, Stanford, CA, 2003), pp. 461–473
- [22] C. Rosales and C. Meneveau, Linear forcing in numerical simulations of isotropic turbulence: Physical space implementations and convergence properties, *Phys. Fluids* **17**, 095106 (2005).
- [23] S. B. Pope, *Turbulent Flows* (Cambridge University Press, Cambridge, UK, 2000).
- [24] C. Canuto, A. Quarteroni, M. Y. Hussaini, and T. A. Zang, *Spectral Methods: Evolution to Complex Geometries and Applications to Fluid Dynamics*, Scientific Computation (Springer, Berlin, 2007).
- [25] C. Canuto, M. Y. Hussaini, A. Quarteroni, and T. A. Zang, *Spectral Methods: Fundamentals in Single Domains*, Scientific Computation (Springer, Berlin, 2006).
- [26] M. Basseigne, J. Urzay, G. I. Park, and P. Moin, Constant-energetics physical-space forcing methods for improved convergence to homogeneous-isotropic turbulence with application to particle-laden flows, *Phys. Fluids* **28**, 035114 (2016).
- [27] K.-S. Choi and J. L. Lumley, The return to isotropy of homogeneous turbulence, *J. Fluid Mech.* **436**, 59 (2001).
- [28] A. J. Simonsen and P.-Å. Krogstad, Turbulent stress invariant analysis: Clarification of existing terminology, *Phys. Fluids* **17**, 088103 (2005).
- [29] M. L. Waite and P. Bartello, Stratified turbulence dominated by vortical motion, *J. Fluid Mech.* **517**, 281 (2004).
- [30] E. Lindborg, The energy cascade in a strongly stratified fluid, *J. Fluid Mech.* **550**, 207 (2006).
- [31] G. Brethouwer, P. Billant, E. Lindborg, and J.-M. Chomaz, Scaling analysis and simulation of strongly stratified turbulent flows, *J. Fluid Mech.* **585**, 343 (2007).
- [32] E. Lindborg and G. Brethouwer, Stratified turbulence forced in rotational and divergent modes, *J. Fluid Mech.* **586**, 83 (2007).
- [33] A. Maffioli, Vertical spectra of stratified turbulence at large horizontal scales, *Phys. Rev. Fluids* **2**, 104802 (2017).
- [34] J. A. Palmore and O. Desjardins, Technique for forcing high Reynolds number isotropic turbulence in physical space, *Phys. Rev. Fluids* **3**, 034605 (2018).
- [35] S. Almalkie and S. M. de Bruyn Kops, Kinetic energy dynamics in forced, homogeneous, and axisymmetric stably stratified turbulence, *J. Turbul.* **13**, N29 (2012).

- [36] C. J. Howland, J. R. Taylor, and C. P. Caulfield, Mixing in forced stratified turbulence and its dependence on large-scale forcing, *J. Fluid Mech.* **898**, A7 (2020).
- [37] E. Bou-Zeid, X. Gao, C. Ansong, and G. G. Katul, On the role of return to isotropy in wall-bounded turbulent flows with buoyancy, *J. Fluid Mech.* **856**, 61 (2018).
- [38] E. C. Itsweire, J. R. Koseff, D. A. Briggs, and J. H. Ferziger, Turbulence in stratified shear flows: Implications for interpreting shear-induced mixing in the ocean, *J. Phys. Oceanogr.* **23**, 1508 (1993).
- [39] P. Billant and J.-M. Chomaz, Self-similarity of strongly stratified inviscid flows, *Phys. Fluids* **13**, 1645 (2001).
- [40] A. Maffioli and P. A. Davidson, Dynamics of stratified turbulence decaying from a high buoyancy Reynolds number, *J. Fluid Mech.* **786**, 210 (2016).
- [41] S. M. de Bruyn Kops and J. J. Riley, The effects of stable stratification on the decay of initially isotropic homogeneous turbulence, *J. Fluid Mech.* **860**, 787 (2019).
- [42] G. P. Chini, G. Michel, K. Julien, C. B. Rocha, and C. P. Caulfield, Exploiting self-organized criticality in strongly stratified turbulence, *J. Fluid Mech.* **933**, A22 (2022).
- [43] T. Passot and A. Pouquet, Numerical simulation of compressible homogeneous flows in the turbulent regime, *J. Fluid Mech.* **181**, 441 (1987).